

Three Axis Attitude Control Using Sliding Mode Based on the Artificial Neural Network for Low Earth Orbit Microsatellite

A.M. Si Mohammed^(a), B. Seba^(a), Y. Bentoutou^(a), N. Taleb^(b), A. Boudjemai^(a), A. Bellar^(a)

^(a)Centre des Techniques Spatiales, Division de Mécanique Spatiale
1, Avenue de la Palestine, Arzew, Algeria

^(b)Djillali Liabes University of Sidi Bel Abbes, Dept. of Electronics, RCAM Laboratory,
Sidi Bel Abbes, Algeria

Abstract—This paper presents the results on the performance of the sliding mode attitude controller for three axis attitude pointing based on the artificial neural network adjusted by a genetic algorithm for low Earth orbit microsatellite. Alsat-1 first Algerian microsatellite had been chosen for this study.

Keywords—Alsat-1, Attitude, Control, Sliding, Artificial, Neural, Network, Genetic, Microsatellite.

I. INTRODUCTION

THE motion of a rigid body in space is specified by its position, velocity, attitude and angular rates. The first two quantities are related to the translational motion of the centre of mass of the spacecraft which is called space navigation, (or orbit determination and control) [1]. The last two parameters are concerned with the rotational motion of the body of the spacecraft about the centre of mass and is the subject of what is called attitude determination and control.

The attitude of a spacecraft is its orientation in space. Attitude analysis may be divided into determination, prediction, and control. Attitude determination is the process of computing the orientation of the spacecraft relative to either an inertial reference or some object of interest such as the Earth. Computation of the orientation of spacecraft with respect to some reference, requires several types of sensors on the spacecraft and sophisticated data processing procedures. The accuracy limit is usually determined by a combination of processing procedures and spacecraft hardware. Attitude prediction is the process of forecasting the future orientation of the spacecraft by using the dynamic models to extrapolate the attitude history. In this case the limiting features are the knowledge of the applied and environmental torques and the accuracy of the mathematical model of the spacecraft dynamics and hardware. Attitude control is the process of orienting the spacecraft in a specified, predetermined direction. It consists of two areas; attitude stabilisation which is the process of maintaining an existing orientation and attitude manoeuvre control, which is the process of controlling the orientation of the spacecraft from one attitude to another.

Since the external (or environmental) disturbing torques can never be eliminated, some form of attitude determination and control is required for nearly all spacecraft. For engineering or flight-related functions,

attitude determination is required only to provide a reference for control. Attitude control is required to avoid solar or atmospheric damage to sensitive components, to control heat dissipation, to point directional antennas and solar panels (for power generation) and to orient thrusters used for orbit manoeuvres. The attitude requirement for spacecraft payloads is more varied and often more stringent than the engineering requirements. Payload requirements, such as antenna orientation, may involve attitude determination, attitude control, or both. Conventionally, a spacecraft is categorised by the procedure by which it is stabilised such as a spin-stabilised spacecraft or a three-axis stabilised spacecraft.

The purpose of the Attitude Determination and Control Subsystem (ADCS) is to stabilise the spacecraft in a desired attitude despite the external disturbance torques acting on it. Stabilisation and control can be accomplished via multiple techniques. These include gravity-gradient, magnetic, pure-spin, dual-spin, one-axis bias momentum, and three-axis stabilisation [1]. The ADCS itself can be grouped into three distinct sections: (a) attitude sensors, (b) actuators, and (c) control logic/control computers. Attitude sensors come in several varieties, including sun sensors, earth-horizon sensors, star sensors, magnetometers, and inertial measurement units (IMUs). There are also several types of actuators, including reaction wheels, momentum wheels, control-moment gyros (CMGs), electromagnetic torquers, and thrusters. Each stabilisation, sensing, and control technique has its own advantages and disadvantages. The optimum combination of stabilisation and control techniques depend largely on the spacecraft system performance requirements imposed on the ADCS, and to a lesser extent, constraints imposed by other satellite subsystems (including the payload).

Alsat-1 is a low-cost microsatellite built by Surrey Satellite Technology Ltd. (SSTL) launched on the 28th of November 2002 from the cosmodrome of Plesetsk in Russia into a 686 km sun synchronous orbit. Alsat-1 is an enhanced Earth microsatellite, stabilised in 3 axis for image acquisition mode. It was designed for disaster monitoring and is part of the international constellation dedicated to Disaster Monitoring (DMC) [2].

This paper presents the design of the sliding mode attitude controller for Alsat-1 based on the artificial neural network adjusted by a genetic algorithm.

The concept of the Genetic Algorithm, first formalized by Holland and extended to functional optimization by Goldberg [3], involves the use of optimization search strategies patterned after the Darwinian notion of natural selection and evolution. During a GA optimization, a set of trial solutions is chosen and evolves toward an optimal solution under the selective pressure of the object function. In general, a GA optimizer must be able to perform five basic tasks encode the solution parameters in the form of chromosomes, initialize a starting population, evaluate and assign fitness values to individuals in the population, perform reproduction through the fitness weighted selection of individuals from the population, and perform recombination and mutation to produce members of the next generation.

This algorithm is represented in Fig. 1.

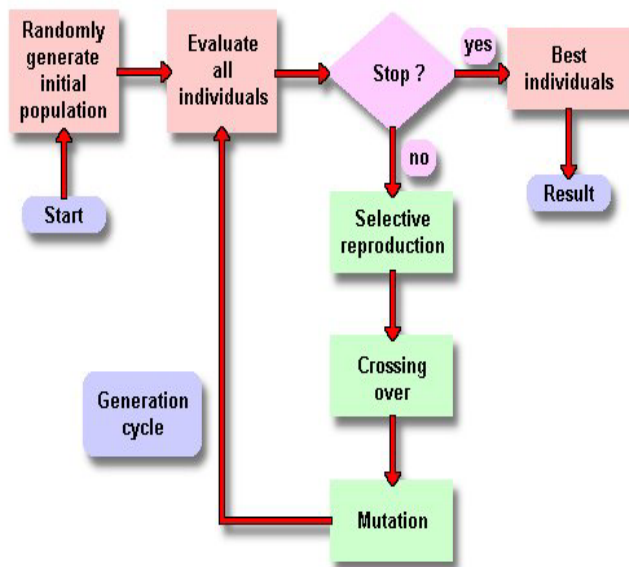


Fig.1: Genetic Algorithm

A. Initialization of the Population

The first step, is to define an initial generation, consists of a set of individuals, each coded by a binary string called genotype (genetic information). These individuals are either defined at the outset or be chosen in a purely random. It is chosen most often for the second possibility because of the realization simplicity [3].

B. Evaluation of the Population

The population estimate is a function called fitness function, which assigns to each individual fitness value to determine the number of times that this individual will be selected for reproduction. This function also represents the link between the physical problem to be solved and the genetic algorithm [3].

C Selection, Reproduction

Each of the individuals is selected by its fitness value. Reproduction consists in duplicating each individual in relation to the average of the performances for all the chromosomes of the population. Then individuals which give the best results have a good probability to be selected for the next generation [3].

D. Crossover

After the reproduction step, a crossover allows a generation of new individuals. The crossover step consists to cut two chromosomes, named parents, on a random place, then the end of these two individuals string is reversed and two chromosomes are created and named children [3].

E. Originality of the Genetic Algorithms

Genetic algorithms present originality compared with other optimization algorithms [3]

- Use encoding parameters.
- Work on a population of points.
- Use the values of the function studied.
- Use the probabilistic transition rules.

F. Advantages and Disadvantages of the Genetic Algorithms

First, the genetic algorithms are expensive in term of computing time, as they handle multiple solutions simultaneously. This is the calculation of the performance function it is most detrimental, and it generally improves the algorithm in order to avoid assessing this function too often. Then, the adjustment of a genetic a algorithm is tricky. One of the most characteristic is that of genetic drift, which is a good person goes in the space of a few generations, to invade the whole population. One speaks in this case premature convergence, which is to launch a local search around a minimum, which is not necessarily the optimum expected. Proportional selection methods may particularly encourage this kind of drift.

Another problem arises when different people start to have similar performance: the good parts are no longer selected, and the algorithm is no longer rising.

The choice of representation "intelligent" to allow an efficient generational replacement is another aspect of the question, and the effectiveness of a genetic algorithm depends heavily on how we operate the crossing of individuals.

The great advantage of genetic algorithms is that they manage to find good solutions to very complex problems, and too remote for conventional combinatorial problems that can take advantage of some known properties. They must simply decide between two alternatives which is better, to make their selections. They are used in areas where a large number of parameters involved, and where one needs to obtain good solutions in a few iterations only.

Moreover, genetic algorithms are well suited because of their simultaneous treatment of solutions in search of optimum multiple: creating a shared cost function, whose value depends partly on the distance between individuals, we see gradually forming sub-populations of individuals, who remain close to various peaks of the objective function. This is the technique of nesting by the method of sharing.

In our search, we use differential evolution algorithms, which are a special case of genetic algorithms that optimize our parameters (synaptic weights of an Artificial Neural Network) are real. Consequently, a differential evolution algorithm does not require an encoding and decoding of individuals to be treated, and it uses all other operations in its process such as selection, crossover and mutation modeled mathematically as functions.

II. ALSAT-1 ATTITUDE DETERMINATION

AND CONTROL SYSTEM

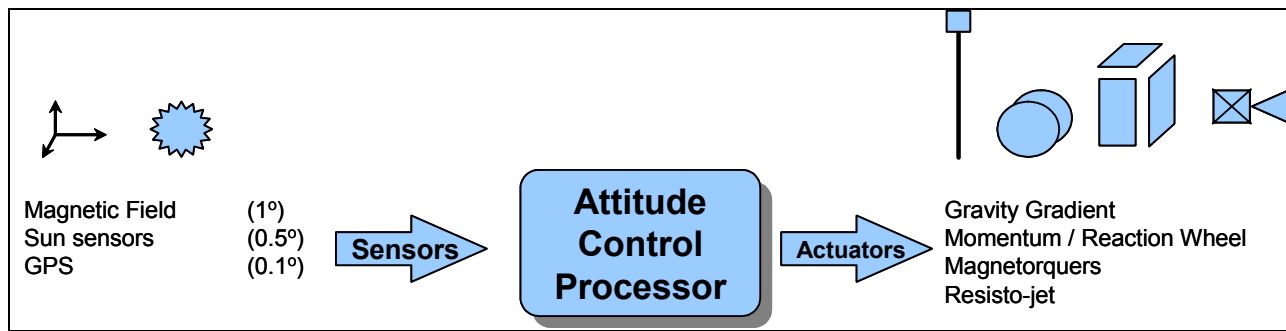


Fig. 2 System diagram & modes of Alsat-1

A. Attitude Sensors

A.1 Magnetometer

Three 3-axis flux gate magnetometers are used to measure the geomagnetic field vector in the satellite's body coordinates. These measurements are used to determine the torque vector generated when switching the magnetorquer coils. When used with a magnetic field model (e.g. IGRF), magnetic measurement and model vectors can be fed to an extended Kalman filter to estimate the full attitude and angular rates of the satellite. For a calibrated magnetometer, during periods of low solar activity, the attitude angles can be estimated to an accuracy of less than 1° per axis. The magnetometer can also be used when the satellite is still tumbling after the launch, to estimate the orbit referenced angular rates of the satellite body by using a rate Kalman filter [4-5].

Table1 presents the Alsat-1 magnetometer characteristics

Table 1 : The Alsat-1 magnetometer characteristics

Power	14 mA @ 12V
Range	- 60 mT to +60 mT
Initial rate during detumbling	< 0.1 deg/s
Full attitude/rate during mission	< 0.5 deg/s
Dimension	130mm X 90mm X 36mm
Mass	295 grm
Thermal characteristics	- 50° C to + 80° C

A.2 SUN SENSORS

Four 2-axis (azimuth and elevation) analogue sun sensors are used to determine the position of the sun relative to the satellite body. Each axis has a ± 60° range and can measure the sun vector to a 1σ accuracy of 0.3° [2]. The four sensors therefore cover the full 360° azimuth range (with an overlap of 30° between sensors) and a 120° elevation range.

Table 2 presents the Alsat-1 sun sensor characteristics

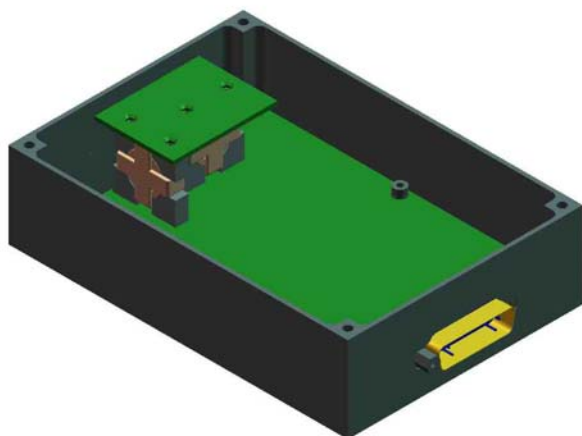


Fig. 3 Magnetometer on Alsat-1

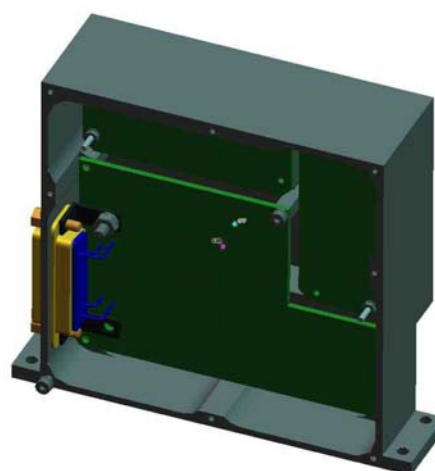


Fig. 4 Sun sensor on Alsat-1

Table 2 : The Alsat-1 sun sensor characteristics

Power	3 mA @ 12V
FOV	+/- 50 deg azimuth/elevation
Accurate knowledge during sun lit	< 0.25 deg
Dimension	90mm X 107mm X 35mm
Mass	300 grm
Thermal characteristics	- 50° C to + 80° C
Vibration tolerance	15 grm RMS

B. ATTITUDE ACTUATORS

B.1 MAGNETORQUERS

The magnetorquers are coils through which a constant current can be switched. Both the polarity (direction) of these current can be controlled to generate on average a magnetic moment vector of any specific magnitude and direction within a defined time interval. The magnetic torquers on Alsat-1 are three magnetorquer rods let say X/Y/Z [2].

The magnetorquer will be used for the following control function on Alsat-1 [6-7]

- Detumbling of the body angular rates after ejection from the launch vehicle;
- Control body spin around orbit normal;
- Libration damping when the GG boom is deployed;
- Yaw phase or yaw angular rate control when the GG boom is deployed;
- Momentum management of the reaction/momentum wheels.

Table 3 presents the Alsat-1 magnetorquer characteristics

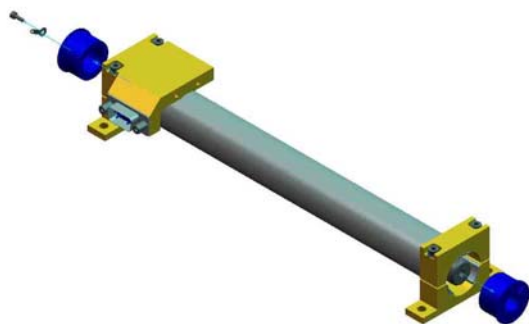


Fig. 5 Magnetorquer on Alsat-1

Table 3 : The Alsat-1 magnetorquer characteristics

Power consumption	500 mW
Mass	500 grm
Dimension	250mmX607mm X38 mm
Thermal characteristics	-30° C to + 60° C

B.2 REACTION/MOMENTUM WHEELS

One momentum wheel is installed in Y axis-axis and two reaction wheels are installed in Z axis (x2 for redundancy). Reaction wheels are essentially torque motors with high-inertia rotors. They can spin in either direction. Roughly speaking one wheel provides for the control of one axis. Momentum wheels are wheels with a nominal spin rate above zero. Their aim is to provide a nearly constant angular momentum. This momentum provides gyroscopic stiffness to two axes, while the motor torque may be controlled to precisely point around the third axis.

The wheels are used for the following control functions on Alsat-1 [7]

- Z-axis wheel (x2 redundancy)
 - Yaw control for push broom;
 - Quick transfer between BBQ mode and yaw steering;
 - Z disturbance cancellation during X thruster firings.
- Y-axis wheel
 - Pitch momentum wheel for 3 axis stabilization with and without boom;
 - Y disturbance cancellation during X thruster firings.

Table 4 presents the Alsat-1 wheel characteristics.

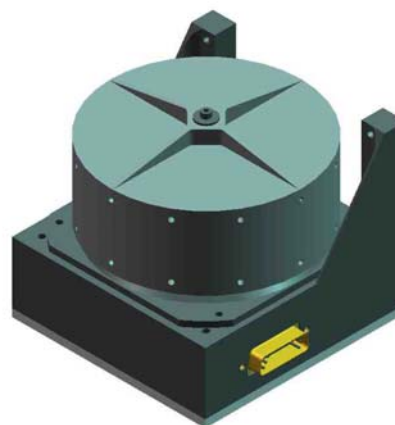


Fig. 6 Wheel on Alsat-1

Table 4 : The Alsat-1 wheel characteristics

Power consumption	0-200 mA @ 28V
	50mA @ 5V
	1.2 W @ constant speed,
	5.0 W @ max. acceleration
	0.8 W @ zero speed
Max. wheel momentum	0.42 Nms
Wheel MOI	0.0008 kgm ²
Max. wheel speed	±5000 rpm

B.3 BOOM

The gravity gradient disturbance is a torque experienced by a low Earth orbiting spacecraft. This disturbance is created by the unsymmetrical mass distribution of the spacecraft, causing a slight difference in the gravity forces acting on the body. The result is a torque around the spacecraft centre of mass.

Table 5 presents the Alsat-1 boom characteristics



Fig. 7 Boom on Alsat-1

Table 5 : The Alsat-1 boom characteristics

Power consumption (Boom controller)	30 ~ 40 mA @ 5V 140 W for 10 msec @ 28V
Boom Length	6 meter
Tip mass	3Kg
Dimension	300mmX200mmX200 mm
Mass (Boom+Tip mass)	5.8kg
Thermal characteristics	-40° C to + 100° C
Vibration tolerance	70 grm

III. ATTITUDE DETERMINATION

The attitude was estimated using a quaternion based extended Kalman filter (qEKF). This filter uses measurement vectors (in the body frame) from all the attitude sensors and by combining them with corresponding modelled vectors (in a reference frame), it estimates the attitude and angular rate values of the satellite.

A 7-state EKF state vector [8-9-10] is comprised of the four-element quaternion attitude vector combined with the three-element body rates vector, with respect to the inertial frame. The state vector to be estimated is 7 dimensional such that

$$\mathbf{x} = [\mathbf{q} \ \boldsymbol{\omega}_B]^T = [q_1 \ q_2 \ q_3 \ q_4 \ \omega_x \ \omega_y \ \omega_z]^T \quad (1)$$

The attitude sensors (magnetometer, sun sensor) will be used to determine the attitude of the satellite relative to the orbital frame. When using magnetic field data: an orbital propagator is used to obtain the position of the satellite. Using this position data, a model of the geomagnetic field, the International Geomagnetic Reference Field (IGRF) model, computes the geomagnetic \mathbf{B} -field in orbit coordinates. On the other hand, the magnetic \mathbf{B} -field is also measured by the 3-axis magnetometer in body coordinates.

The attitude can then be solved from these two vectors over time. The innovation value used in the EKF is the vector difference between the measured body referenced vector and a modelled orbit referenced vector, (see Fig. 8), transformed to the body frame by the estimated attitude transformation matrix.

$$\mathbf{e}(k) = \mathbf{v}_{\text{meas}}(k) - \mathbf{A}[\hat{\mathbf{q}}(k)]\mathbf{v}_{\text{orb}}(k) \quad (2)$$

$$\mathbf{v}_{\text{meas}}(k) = \frac{\mathbf{B}_{\text{meas}}(k)}{\|\mathbf{B}_{\text{meas}}(k)\|} \quad (3)$$

$$\mathbf{v}_{\text{orb}}(k) = \frac{\mathbf{B}_{\text{orb}}(k)}{\|\mathbf{B}_{\text{orb}}(k)\|} \quad (4)$$

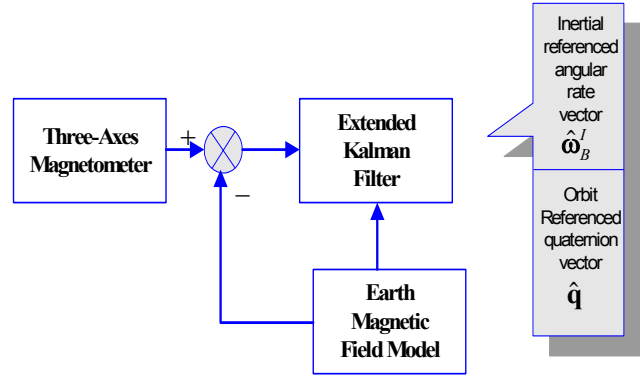


Fig. 8 Magnetic Attitude Estimate Procedure using a qEKF

The system equation implemented on board Alsat-1 is given by [8-9-10]

$$\dot{\mathbf{q}} = \frac{1}{2} \begin{bmatrix} 0 & \omega_{oz} & -\omega_{oy} & \omega_{ox} \\ -\omega_{oz} & 0 & \omega_{ox} & \omega_{oy} \\ \omega_{oy} & -\omega_{ox} & 0 & \omega_{oz} \\ -\omega_{ox} & -\omega_{oy} & -\omega_{oz} & 0 \end{bmatrix} \begin{bmatrix} q_1 \\ q_2 \\ q_3 \\ q_4 \end{bmatrix} \quad (5)$$

$$\dot{\boldsymbol{\omega}}_{BY} = \begin{bmatrix} \dot{\omega}_x \\ \dot{\omega}_y \\ \dot{\omega}_z \end{bmatrix} = \begin{bmatrix} \frac{N_x^{MT}}{I_x} + 3\omega_0^2 \alpha a_{23} a_{33} - \alpha \omega_y \omega_z \\ -\frac{h_z}{I_x} \omega_y + \frac{h_y}{I_x} \omega_z - \frac{\dot{h}_x}{I_x} + w_x \\ \frac{N_y^{MT}}{I_y} + 3\omega_0^2 \beta a_{13} a_{33} - \beta \omega_x \omega_z \\ -\frac{h_x}{I_y} \omega_z + \frac{h_z}{I_y} \omega_x - \frac{\dot{h}_y}{I_y} + w_y \\ \frac{N_z^{MT}}{I_z} + 3\omega_0^2 \gamma a_{13} a_{23} - \gamma \omega_x \omega_y \\ -\frac{h_y}{I_z} \omega_x + \frac{h_x}{I_z} \omega_y - \frac{\dot{h}_z}{I_z} + w_z \end{bmatrix} \quad (6)$$

where,

$\boldsymbol{\omega}_{BY} = [\omega_x \ \omega_y \ \omega_z]^T$: inertially referenced body angular rate vector;

$\boldsymbol{\omega}_{LO} = [\omega_{ox} \ \omega_{oy} \ \omega_{oz}]^T$: orbit reference body angular velocity vector;

$\mathbf{q} = [q_1 \ q_2 \ q_3 \ q_4]^T$: quaternion;

$\mathbf{N}^{MT} = [N_x^{MT} \ N_y^{MT} \ N_z^{MT}]^T$: applied torque vector by

3-axis magnetorquers;

$\mathbf{w} = [w_x \ w_y \ w_z]^T$: zero mean system noise vector;

a_{ij} : (i,j) component of the DCM matrix;

$$\alpha = \frac{I_z - I_y}{I_x}, \beta = \frac{I_x - I_z}{I_y}, \gamma = \frac{I_y - I_x}{I_z}.$$

The Kalman filter algorithm is given as follows [8-9]

Propagation Cycle

- Covariance Propagation

$$\Phi_{k+1} \approx \mathbf{I}_{7 \times 7} + \begin{bmatrix} \frac{\partial \hat{\mathbf{q}}}{\partial \mathbf{q}} & \frac{\partial \hat{\mathbf{q}}}{\partial \boldsymbol{\omega}} \\ \frac{\partial \hat{\boldsymbol{\omega}}}{\partial \mathbf{q}} & \frac{\partial \hat{\boldsymbol{\omega}}}{\partial \boldsymbol{\omega}} \end{bmatrix} \Delta t \quad (7)$$

$$\bar{\mathbf{P}}_{k+1} = \Phi_{k+1} \hat{\mathbf{P}}_k \Phi_{k+1}^T + \mathbf{Q}_k \quad (8)$$

The process noise covariance matrix \mathbf{Q} implemented on board Alsat-1 is given by [8-9]

$$\mathbf{Q} \approx \text{diag} \left[\begin{array}{c} \frac{\sigma^2}{12} \left(\frac{q_4^2}{I_x^2} + \frac{q_3^2}{I_y^2} + \frac{q_2^2}{I_z^2} \right) \Delta t^3 \quad \frac{\sigma^2}{12} \left(\frac{q_3^2}{I_x^2} + \frac{q_4^2}{I_y^2} + \frac{q_1^2}{I_z^2} \right) \Delta t^3 \\ \frac{\sigma^2}{12} \left(\frac{q_2^2}{I_x^2} + \frac{q_1^2}{I_y^2} + \frac{q_4^2}{I_z^2} \right) \Delta t^3 \quad \frac{\sigma^2}{12} \left(\frac{q_1^2}{I_x^2} + \frac{q_2^2}{I_y^2} + \frac{q_3^2}{I_z^2} \right) \Delta t^3 \\ \frac{\sigma^2}{I_x^2} \Delta t \quad \frac{\sigma^2}{I_y^2} \Delta t \quad \frac{\sigma^2}{I_z^2} \Delta t \end{array} \right] \quad (9)$$

- Propagate State

$$\bar{\mathbf{X}}_{k+1} = \hat{\mathbf{X}}_k + \int_{t_k}^{t_{k+1}} \dot{\mathbf{X}} dt \quad (10)$$

specifically

$$\bar{\mathbf{q}}_{k+1} = \hat{\mathbf{q}}_k + \int_{t_k}^{t_{k+1}} (\boldsymbol{\Omega} \mathbf{q}) dt \quad (11)$$

$$\bar{\boldsymbol{\omega}}_{k+1} = \hat{\boldsymbol{\omega}}_k + \int_{t_k}^{t_{k+1}} \mathbf{I}^{-1} [\mathbf{N} - \boldsymbol{\omega} \times (\mathbf{I} \boldsymbol{\omega} + \mathbf{h}) - \dot{\mathbf{h}}] dt \quad (12)$$

Correction Cycle

- Compute Observation Matrix

$$\mathbf{H}_k = \begin{bmatrix} \frac{\partial \mathbf{A}}{\partial q_1} \mathbf{Z}_{LO} & \frac{\partial \mathbf{A}}{\partial q_2} \mathbf{Z}_{LO} & \frac{\partial \mathbf{A}}{\partial q_3} \mathbf{Z}_{LO} & \frac{\partial \mathbf{A}}{\partial q_4} \mathbf{Z}_{LO} & \mathbf{0}_{3 \times 3} \end{bmatrix} \quad (13)$$

Compute Kalman Gain Matrix

$$\mathbf{K}_k = \mathbf{P}_k \mathbf{H}_k^T (\mathbf{H}_k \mathbf{P}_k \mathbf{H}_k^T + \mathbf{R}_k)^{-1} \quad (14)$$

Update State

$$\hat{\mathbf{X}}_{k+1} = \bar{\mathbf{X}}_{k+1} + \mathbf{K}_{k+1} (\mathbf{Z}_{BY} - \mathbf{A} \mathbf{Z}_{LO}) \quad (15)$$

Update Covariance

$$\hat{\mathbf{P}}_{k+1} = [\mathbf{I}_{7 \times 7} - \mathbf{K}_{k+1} \mathbf{H}_{k+1}] \bar{\mathbf{P}}_{k+1} \quad (16)$$

The Kalman filter loop process is depicted in Fig. 9

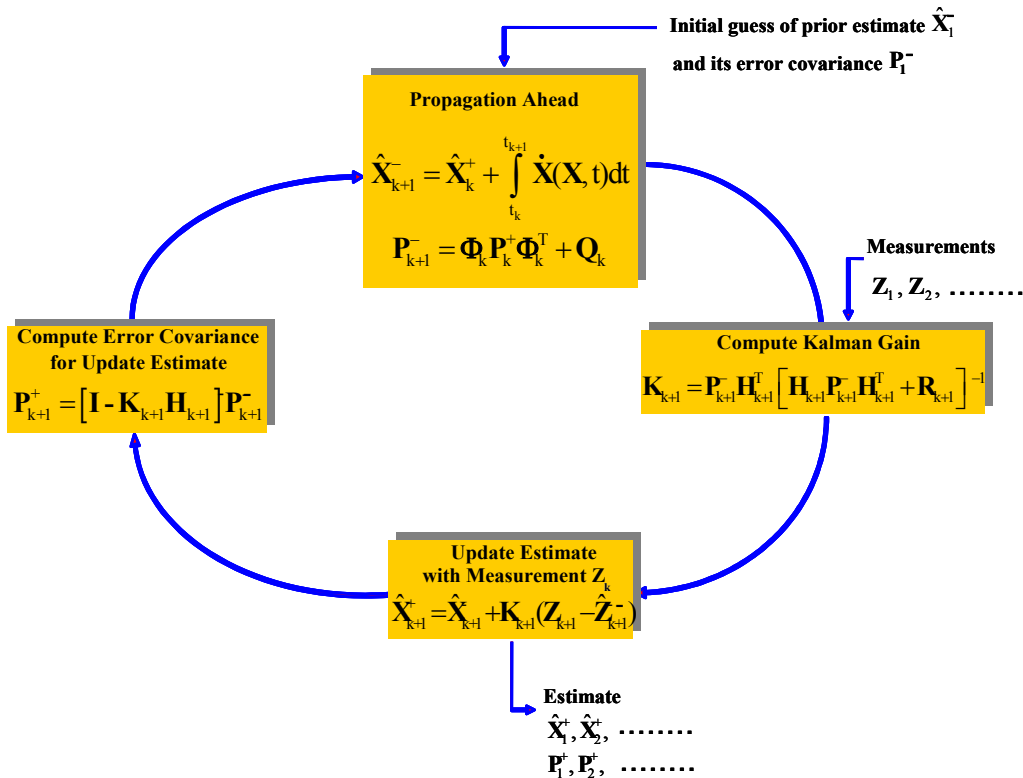


Fig. 9 Kalman Filter Loop Process

where,

- P** : Covariance matrix (7x7);
- K** : Kalman gain matrix (7x3);
- Φ** : State transformation matrix (7x7) ;
- R** : Measurement noise covariance matrix (3x3);
- Q** : Process noise covariance matrix (7x7) ;
- H** : Observation matrix (7x7);
- F** : Mathematical convention (7x7);
- Z** : Measurements of system state, either sun-sensor or magnetometer;
- Z_{BY}** : Body referenced measurements, directly from onboard sensors;
- Z_{LO}** : Orbit referenced measurements, from orbit model prediction;
- t** : time.

IV. ATTITUDE CONTROL

This section will be devoted to the problem of the attitude control using reaction wheels based on the sliding mode control. Since the attitude quaternion has three independent components, this implies that we must find three sliding surfaces.

The sliding mode control [11] has largely proved its effectiveness in the field of robotics, electric machinery, etc The benefit of such control is its robustness against disturbances and model uncertainties. Every time she has a major drawback is the chattering phenomenon [11].

The implementation of the sliding mode control law is performed in three steps as follows
Step 1: choice of sliding surface;
Step 2: Convergence condition and existence;
Step 3: Establishment of the control law.

Recall the dynamic of the spacecraft in the inertial space which is governed by Euler's equations of motion [1].

$$\mathbf{I}\dot{\boldsymbol{\omega}}_B^I = \mathbf{C} - \boldsymbol{\omega}_B^I \times (\mathbf{I}\boldsymbol{\omega}_B^I + \mathbf{h}) - \dot{\mathbf{h}} \quad (17)$$

where,

$$\boldsymbol{\omega}_B^I = [\omega_x \quad \omega_y \quad \omega_z]^T \quad \text{: inertially referenced body}$$

angular rate vector;

$$\mathbf{I} = \begin{bmatrix} I_{xx} & I_{xy} & I_{xz} \\ I_{yx} & I_{yy} & I_{yz} \\ I_{zx} & I_{zy} & I_{zz} \end{bmatrix} \quad \text{: moment of inertia tensor of}$$

spacecraft (MOI);

$$\mathbf{h} = [h_x \quad h_y \quad h_z]^T \quad \text{: reaction wheel angular}$$

momentum vector;

$$\mathbf{C}_D = [C_{dx} \quad C_{dy} \quad C_{dz}]^T \quad \text{: external disturbance torque}$$

vector such as aerodynamic torque and solar radiation pressure torque.

Let $\mathbf{U} = -\dot{\mathbf{h}} - \boldsymbol{\omega} \times \mathbf{h}$ the control torque generated by the 3 reaction wheels for 3-axis active attitude control.

We propose the following sliding surface

$$\mathbf{S} = \dot{\mathbf{q}}_e + \mathbf{W} \mathbf{q}_e \quad (18)$$

where,

$\mathbf{q}_e = \mathbf{q}_c \mathbf{q}$: quaternion error;

\mathbf{W} : diagonal gain matrix (3×3) .

Deriving Equation (18), yields

$$\dot{\mathbf{S}} = \ddot{\mathbf{q}}_e + \mathbf{W} \dot{\mathbf{q}}_e = \mathbf{q}_c \ddot{\mathbf{q}} + \mathbf{W} \mathbf{q}_c \dot{\mathbf{q}} \quad (19)$$

Assuming

$$\dot{\mathbf{S}} = \mathbf{0} \quad (20)$$

Then

$$\mathbf{q}_c \ddot{\mathbf{q}} = -\mathbf{W} \mathbf{q}_c \dot{\mathbf{q}} \quad (21)$$

On the other hand, we have

$$\ddot{\mathbf{q}} = \dot{\boldsymbol{\Lambda}} \boldsymbol{\omega} + \boldsymbol{\Lambda} \dot{\boldsymbol{\omega}} \quad (22)$$

Substituting Equation (17) into Equation (22) yields

$$\ddot{\mathbf{q}} = \dot{\boldsymbol{\Lambda}} \boldsymbol{\omega} + \boldsymbol{\Lambda} \mathbf{I}^{-1} (-\boldsymbol{\omega} \times \mathbf{I} \boldsymbol{\omega} + \mathbf{U}_{eq} + \mathbf{C}) \quad (23)$$

Where again

$$\mathbf{q}_c \dot{\boldsymbol{\Lambda}} \boldsymbol{\omega} + \mathbf{q}_c \boldsymbol{\Lambda} \mathbf{I}^{-1} (-\boldsymbol{\omega} \times \mathbf{I} \boldsymbol{\omega} + \mathbf{U}_{eq} + \mathbf{C}) = -\mathbf{W} \mathbf{q}_c \dot{\mathbf{q}} \quad (24)$$

Result

$$\mathbf{U} = -(\mathbf{q}_c \boldsymbol{\Lambda} \mathbf{I}^{-1})^{-1} \left[\mathbf{q}_c \dot{\boldsymbol{\Lambda}} \boldsymbol{\omega} + \mathbf{W} \mathbf{q}_c \dot{\mathbf{q}} + \mathbf{q}_c \boldsymbol{\Lambda} \mathbf{I}^{-1} (\mathbf{C} - \boldsymbol{\omega} \times \mathbf{I} \boldsymbol{\omega}) \right] \quad (25)$$

Finally the sliding mode control is given as follows

$$\mathbf{U} = -(\mathbf{q}_c \boldsymbol{\Lambda} \mathbf{I}^{-1})^{-1} \left[\mathbf{q}_c \dot{\boldsymbol{\Lambda}} \boldsymbol{\omega} + \mathbf{W} \mathbf{q}_c \dot{\mathbf{q}} + \mathbf{q}_c \boldsymbol{\Lambda} \mathbf{I}^{-1} (\mathbf{C} - \boldsymbol{\omega} \times \mathbf{I} \boldsymbol{\omega}) \right] - \mathbf{K} \sin g(\mathbf{S}) \quad (26)$$

To eliminate the chattering phenomenon, the function is replaced by a smooth function.

V. SIMULATIONS RESULTS

For this application, the sliding mode controller based on the artificial neural network adjusted by a hybrid algorithm is simulated. We used a combination of two algorithms (Levenberg-Marquardt differential evolution) whose source code is available in Matlab on the Internet [12]. The differential evolution algorithm is used as pre-learning Levenberg-Marquardt. The differential evolution attempts to obtain a good solution by gradually reducing the search space. The Levenberg-Marquardt uses this solution to find an optimal solution more accurate.

The main objective here is to find the best learning can provide a good model. For this, several tests are necessary, acting on the parameters affecting the learning. The simulation parameters are given in the following Tables.

Table 6: The artificial neural network structure

Structure	Multilayer recurrent network
Number of hidden layers	1
Number of neurons in each hidden layer	3
Activation functions of hidden layers	tansig
Number of training samples	24000
Learning method	Gradient error back propagation

Table 7: The evolutionary algorithm parameters

Initial population	2
Crossover rate	0.9
Constant mutation	0.7
Stopping criterion	50 Generations
	Accuracy of 10^{-5}

The following initialization attitude parameters were utilized during the simulation

Table 8: Orbit characteristics

Orbit	Circular
Inclination [degree]	98
Altitude [km]	680
sampling period [sec]	10

Table 9: Initial Euler angles and rates for the attitude propagator

Initial roll angle ϕ [degree]	10
Initial pitch angle θ [degree]	10
Initial yaw angle ψ [degree]	-5
Initial angular rate ω_{ox} [degree/sec]	0
Initial angular rate ω_{oy} [degree/sec]	-0.06
Initial angular rate ω_{oz} [degree/sec]	0.0

Table 10: Initial Euler angles and rates for the attitude filter (qEKF)

Initial roll angle ϕ [degree]	0.0
Initial pitch angle θ [degree]	0.0
Initial yaw angle ψ [degree]	0.0
Initial angular rate ω_{ox} [degree/sec]	0.0
Initial angular rate ω_{oy} [degree/sec]	-0.06
Initial angular rate ω_{oz} [degree/sec]	0.0

Table 11: Inertia tensor (Satellite configuration I)

I_{xx} [kgm ²]	152.9
I_{xy} [kgm ²]	0.0
I_{xz} [kgm ²]	0.0
I_{yx} [kgm ²]	-0.25
I_{yy} [kgm ²]	152.5
I_{yz} [kgm ²]	0.0005
I_{zx} [kgm ²]	0.1
I_{zy} [kgm ²]	0.0
I_{zz} [kgm ²]	4.91

Table 12: Miscellaneous

Simulation time [orbit]	3.0
Integration step [sec]	0.1
Sampling time [sec]	1

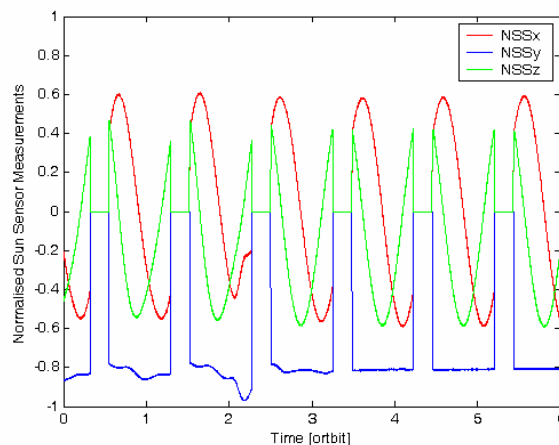


Fig. 10 Sun sensor measurement during three axis attitude pointing control

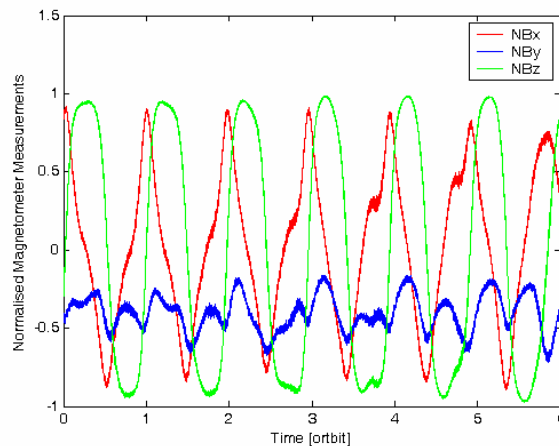


Fig. 11 Magnetometer measurement during three axis attitude pointing control

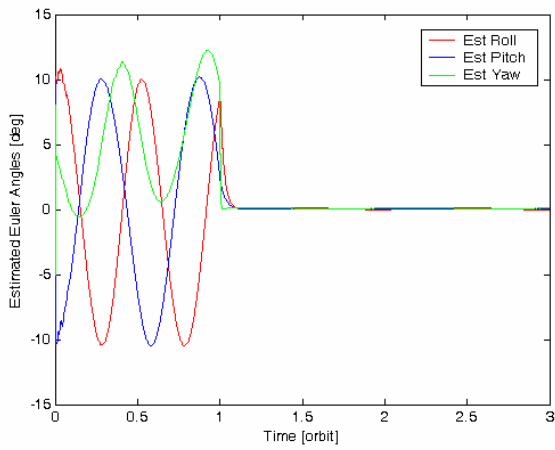


Fig. 12 Estimated Euler angles during three axis attitude pointing control

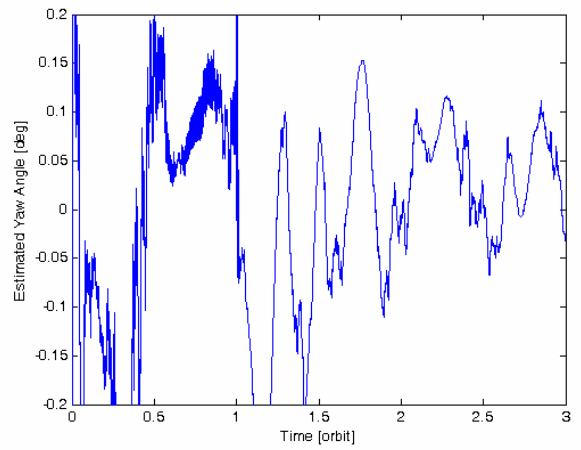


Fig. 15 Estimated yaw angle during three axis attitude pointing control

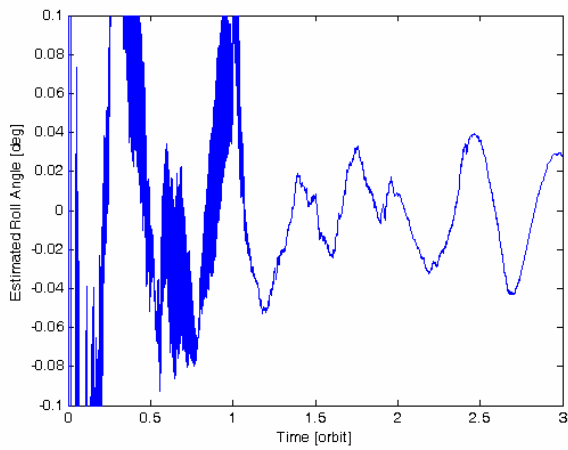


Fig. 13 Estimated roll angle during three axis attitude pointing control

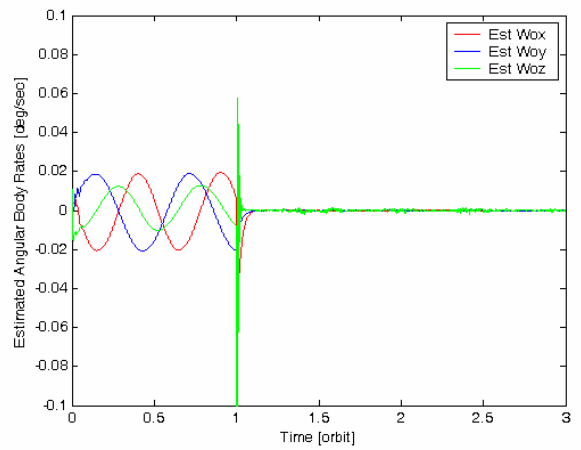


Fig. 16 Estimated angular body rates during three axis attitude pointing control

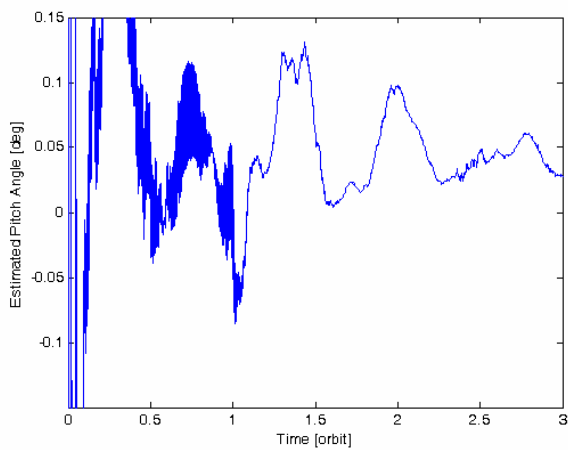


Fig. 14 Estimated pitch angle during three axis attitude pointing control

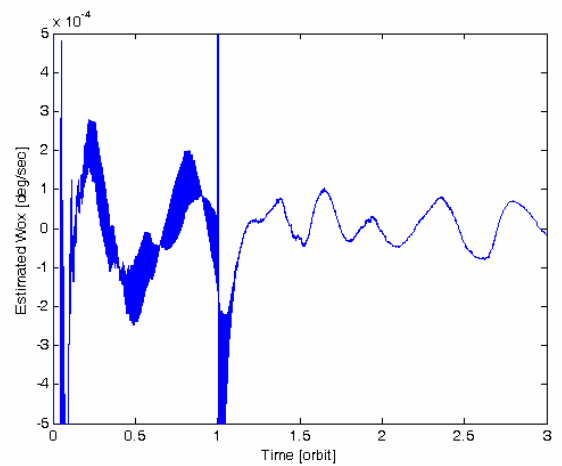


Fig. 17 Estimated angular body rate ω_{ox} during three axis attitude pointing control

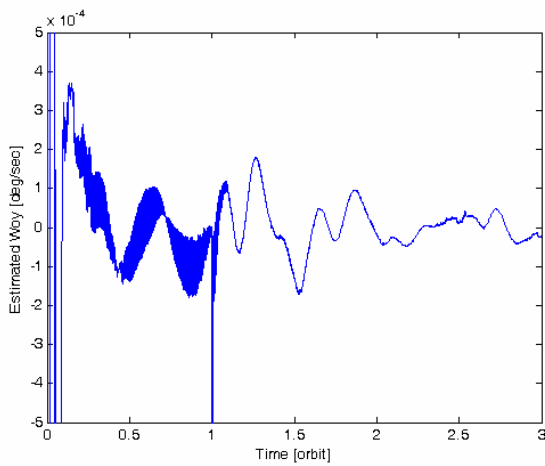


Fig. 18 Estimated angular body rate ω_{oy} during three axis attitude pointing control

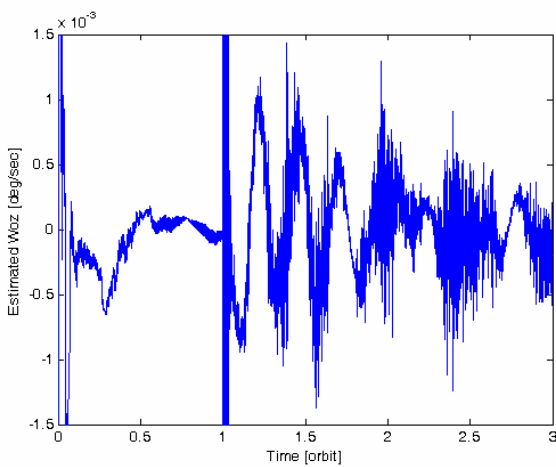


Fig. 19 Estimated angular body rate ω_{oz} during three axis attitude pointing control

The state error estimation and the RMS of attitude parameters during three axis attitude pointing control are computed at the third orbit and presented by the following tables.

Table 13: State error estimation during three axis attitude pointing control

	RMS of attitude error
Roll [deg]	0.025
Pitch [deg]	0.068
Yaw [deg]	0.11
ω_{ox} [deg/sec]	$6.42 \cdot 10^{-5}$
ω_{oy} [deg/sec]	$7.80 \cdot 10^{-5}$
ω_{oz} [deg/sec]	$3.57 \cdot 10^{-4}$
	Magnitude of error
Angles [deg]	0.13
Angular velocity [deg/sec]	$3.71 \cdot 10^{-4}$

Table 14: RMS of attitude parameters during three axis attitude pointing control

	RMS of attitude parameters
Roll [deg]	0.08
Pitch [deg]	0.05
Yaw [deg]	0.09
ω_{ox} [deg/sec]	$6.30 \cdot 10^{-5}$
ω_{oy} [deg/sec]	$2.45 \cdot 10^{-5}$
ω_{oz} [deg/sec]	$4.05 \cdot 10^{-4}$
	Magnitude of error
Angles [deg]	0.13
Angular velocity [deg/sec]	$4.10 \cdot 10^{-4}$

Figures 12 to 19 show the simulation result when doing three axis attitude pointing control with a deployed boom using the reaction wheels. The satellite is left to nutate freely for the second orbit, starting from an initial attitude of 10 deg pitch, 10 deg roll and -5 deg yaw. At the start of the first orbit the three reaction wheels are activated and within a fraction of an orbit the pitch and roll librations are damped to a three axis attitude pointing error less than 0.15 deg and 0.4 mdeg/sec.

It can be seen from Table 8 that the magnitude of the RMS error estimation when using the 7-state EKF indicates that the angular error is approximately 0.13 deg. The rate error is about 0.37 mdeg/sec.

The artificial neural network controller adjusted by the differential evolution algorithm initially based on the sliding mode has completed its task for three axis attitude pointing control, while keeping the performance of the Artificial Neural Network.

VI. CONCLUSION

This paper presents the results on the performance of the sliding mode attitude controller for three axis attitude pointing based on the artificial neural network adjusted by a genetic algorithm for an active gravity gradient stabilised microsatellite. The technique consists with used the genetic algorithm to determine the optimal attitude controller. This algorithm has the advantage of escaping the local solutions, it tend to produce global optimal results without requiring a great deal of information about the solution domain. However, the choice of the function fitness is delicate, because it is the only link between the physical problem to optimize and the genetic algorithm.

The artificial neural network controller initially adjusted by the differential evolution algorithm which is a special case of genetic algorithm has completed its task for three axis attitude pointing control error less than 0.15 deg and 0.4 mdeg/sec.

To conclude, the attitude control based on the genetic algorithm can be attractive, efficient, alternative attitude control systems for an active gravity gradient stabilised satellite but it can be extended for agile satellite.

REFERENCES

- [1] J.R. Wertz, *Spacecraft Attitude Determination and Control*, D. Reidel Publishing Company, Dordrecht, The Nederland, 1985.
- [2] A.M. Si Mohammed, M.N. Sweeting, J. R. Cooksley, "An Attitude Determination and Control System of the Alsat-1 First Algerian Microsatellite", Proceeding IEEE Recent Advances in Space Technologies, RAST 2003, 20-22 November, 2003, Istambul, Turkey.
- [3] D.E. Goldberg, *Genetic Algorithm Search, Optimization and Machine Learning*, Addison-Wesley 1994.
- [4] A. Gelb, *Applied Optimal Estimation*, The M.I.T. Press, Cambridge - Massachusetts - London, 1988.
- [5] R.G. Brown, P.Y.C. Hwang, *Introduction to Random Signals and Applied Kalman Filtering*, John Wiley and Sons, New York - Chichester - Brisbane - Toronto - Singapore, 1992.
- [6] A.M. Si Mohammed, M. Benyettou, S. Chouraqui, A. Boudjemai, Y. Hashida, "Magnetorquer Control for Orbital Manoeuvre of Low Earth Orbit Macrosatellite", Journal of WSEAS Transactions on Communications, Vol. 5, Issue 5, pp. 944-947, May 2006.
- [7] A.M. Si Mohammed, M. Benyettou, Y. Bentoutou, Y. Hashida, M.N. Sweeting. "Three-Axis Active Control System for Gravity Gradient Stabilised Microsatellite". Acta Astronautica. Vol. 64, N°7, pp. 796 - 809, April 2009.
- [8] A.M. Si Mohammed, A. Boudjemai, M. Benyettou, Y. Hashida, "Seven State Kalman Filtering for LEO Microsatellite Attitude Determination" Recent Advances in Signal Processing, Robotics and Automation. Cambridge University, Feb. 2010, ISBN: 978-960-474-157-1, ISSN: 1790-5117, pp. 151-157.
- [9] A.M. Si Mohammed, *Kalman Filtering. Attitude Determination using Kalman Filtering for Low Earth Orbit Microsatellites*. Book Chapter, Nova Publishers, NY, USA, pp. 161-196, 2011.
- [10] Y. Hashida, *ADCS Design for Future UoSAT Standard Platform*, Surrey Space Centre, Guilford, UK, August 2004.
- [11] J. Slotin, W. Li, *Applied Nonlinear Control*, Englewood Cliffs, Prince Hall, 1991.
- [12] <http://it.lut.fi/project/nngenetic/>.